ADVANCED FUNCTIONAL MATERIALS
www.afm-journal.de

www.MaterialsViews.com

Vapor Phase Growth of Functional Pentacene Films at Atmospheric Pressure

Cédric Rolin, Karolien Vasseur, Björn Niesen, Myriam Willegems, Robert Müller, Sören Steudel, Jan Genoe, and Paul Heremans*

Compared to traditional vacuum evaporation techniques for small organic molecules, organic vapor phase deposition (OVPD) possesses a extra processing parameter: the pressure of process gas P_{ch}. Here, the influence of large P_{ch} variations (from 0.1 mbar to atmospheric pressure) on pentacene thin film growth is explored. OVPD operation at higher P_{ch} is characterized by lower carrier gas velocities and lower organic diffusivities. These result in an invariance of the material utilization efficiency over the entire pressure span and in an advantageous equilibrium evaporation regime in the source. An increase in P_{ch} yields rough pentacene layers. Classical nucleation theory is applied to demonstrate how the pressure rise triggers homogeneous nucleation in the gas phase, causing the observed roughening. The use of lower deposition rates, higher dilution flow rates, and higher substrate temperatures result in the suppression of gas phase nucleation and the growth of smooth pentacene films at atmospheric pressure. Using these optimized conditions, state-of-the-art pentacene thin film transistors with saturation mobilities above 0.9 cm^2/Vs are reproducibly fabricated. p-Type circuits are also made and a 19-stage ring oscillator with a stage delay of 51 μs at a supply voltage of 15 V is demonstrated.

1. Introduction

Depending on the medium used to apply molecules into a functional thin film, small molecular organic semiconductors can be processed either in liquid or in vapor phase. Considering vapor phase techniques, vacuum thermal evaporation (VTE) has rapidly imposed itself as a standard for thin film formation of small molecular organic semiconductors. It is able to deposit multilayers of most small-molecular organic materials with a high purity and uniformity.[1] However, this technique suffers from limited options in patterning and complex upscaling.[2]

Alternative vapor phase techniques have emerged that rely on a carrier gas to dilute and transport the evaporated organic molecules from a source cell to a cooled substrate on which they condense. The physical separation between the evaporation and condensation phenomena has given rise to varied system architectures. In organic vapor phase deposition (OVPD),[3,4] the entire substrate surface is exposed to the process gas loaded with organic molecules, relying on a showerhead (SH) in some instances to finely control fluid flow patterns. OVPD has been demonstrated to uniformly grow complex multilayer structures over large area substrates at high speeds.[5–7] In organic vapor jet printing (OVJP), the process gas is jetted onto the substrate, using a nozzle or an array of nozzles.[8,9] OVJP can deposit functional multilayered organic dots at unprecedented speeds, giving access to direct layer patterning.

The use of a carrier gas adds a new growth parameter in OVPD and OVJP: the pressure in the deposition chamber (P_{ch}), which is usually held between 0.1 and 10 mbar. In OVJP, due to high gas speeds at the nozzle exit, mass transport remains essentially convective giving rise to a kinetic growth that is not much affected by background pressures. Functional dots have been grown by OVJP at atmospheric pressure.[8,10] In contrast, in OVPD, the growth is mostly limited by the diffusion of organic species through a boundary layer (BL) of carrier gas formed on the substrate surface.[11] In this case, growth takes place closer to equilibrium and is impacted by the carrier gas pressure.[6] However this effect has not been much documented so far. In this work, we study how pressure affects the growth by OVPD of a standard polycrystalline organic semiconductor, pentacene.[12] We unveil some of the mechanisms of morphological evolution with pressure and demonstrate a successful process window to grow smooth and functional pentacene films at atmospheric pressure.

2. Results and Discussion

This section is organized as follows. In the first subsection, the effects of a pressure rise on the mass transport in OVPD

Dr. C. Rolin, K. Vasseur, B. Niesen, M. Willegems, Dr. R. Müller, Dr. S. Steudel, Prof. J. Genoe, Prof. P. Heremans
imec, Polymer and Molecular Electronics Group
Kapeldreef, 75, B-3001 Leuven, Belgium
E-mail: cedric.rolin@gmail.com
K. Vasseur
Katholieke Universiteit Leuven
Department of Metallurgy and Materials Engineering
Kasteelpark Arenberg, 44, B-3001 Leuven, Belgium
B. Niesen, Prof. P. Heremans
Katholieke Universiteit Leuven
Department of Electrical Engineering
Kasteelpark Arenberg, 10, B-3001 Leuven, Belgium

DOI: 10.1002/adfm.201200896

© 2012 WILEY-VCH Verlag GmbH & Co. KGaA, Weinheim

are described. Next, we show how this pressure rise results in an extreme thin film roughening that is detrimental for pentacene thin film electrical characteristics. The next subsection discusses the origin of this roughening through an analysis of the gas phase nucleation process. By understanding the roots of roughening, we then demonstrate a process window where smooth pentacene films can be grown at atmospheric pressure. Following this optimization process, functional pentacene thin films grown at atmospheric pressure are presented in the final subsection that are used to fabricate state-of-the-art organic circuitry.

2.1. Effect of Pressure on Mass Transport in the OVPD System

In order to conduct this study, the pressure range of the OVPD system described in ref. [13] is extended over four decades, from a chamber pressure P_{ch} of 0.1 mbar up to 1200 mbar by adding a removable constriction along the pump line that radically decreases pump speed in the deposition chamber. Besides P_{ch}, other OVPD process parameters are the furnace temperature T_{fur} (set between 230 to 290 °C), the substrate temperature T_{sub} (adjusted from 25 to 105 °C), the source carrier gas flow rate q_s (varying from 25 to 500 sccm, standard cube centimeter per minute). Finally, in order to ensure a uniform operation of the showerhead, the source flow is diluted with some supplementary carrier gas. This sets the total carrier gas flow rate q_{tot} (set between 100 and 5000 sccm). A schematic drawing of the system is given in **Figure 1**, where all process parameters defined above are indicated along with other system parameters used later. This drawing shows how the SH and piping physically separate the chamber from the source cell loaded with a powder of the organic material. This separation leads to a certain independence of the evaporation and condensation processes. The source usually operates out of equilibrium whereas the condensation process is known to be diffusion limited due to the formation of the carrier gas BL on top of the substrate.[11]

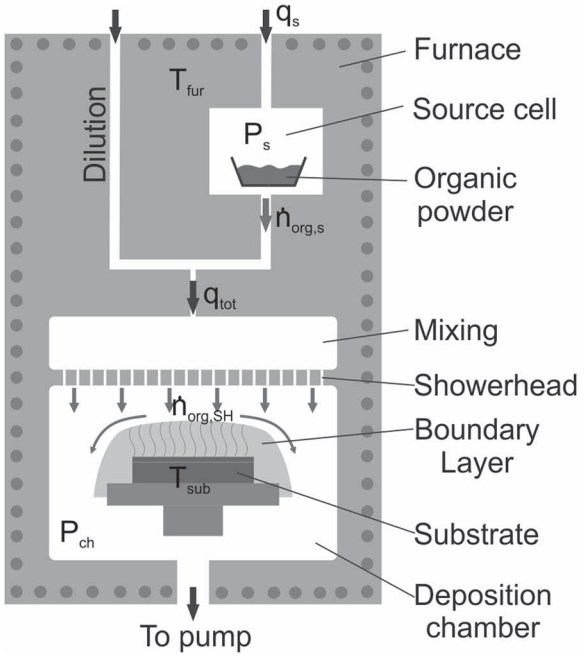

Figure 1. Schematic drawing of the OVPD system used in this study.

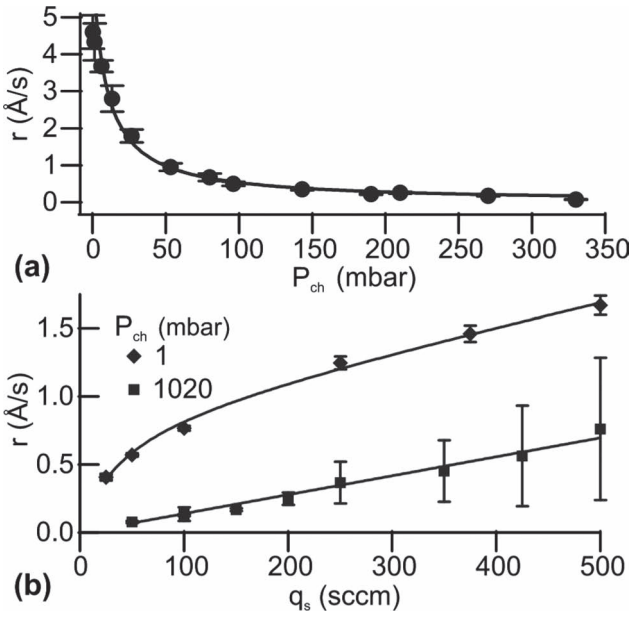

Figure 2. a) Deposition rate r as a function of chamber pressure P_{ch}. $T_{fur} = 250$ °C, $T_{sub} = 65$ °C, $q_s = 50$ sccm and $q_{tot} = 100$ sccm. Measured rates are fitted using Equation 1. b) Deposition rate r versus source cell flow rate q_s at $P_{ch} = 1$ mbar (diamonds) and $P_{ch} = 1020$ mbar (squares). $T_{fur} = 255$ °C, $T_{sub} = 65$ °C and $q_{tot} = 1000$ sccm. Measured rates are fitted using, respectively, Equation 1 and 2. The large error bars on the data at atmospheric pressure are due to film roughness that complicates thickness measurements.

While exploring high pressures in OVPD, a first task is to understand how P_{ch} affects the system behavior, in particular its deposition rate r and its material utilization efficiency η. **Figure 2** shows how r, obtained from an ex situ pentacene thickness measurement, evolves with P_{ch} (Figure 2a) and with q_s at low pressure (Figure 2b, diamonds) and at atmospheric pressure (Figure 2b, squares). These trends can be interpreted by examining Equation (1) that relates r to different process parameters:

$$r = \frac{\eta}{A_{sub}\rho_{org}}\dot{n}_{org,SH} = \frac{\eta}{A_{sub}\,\rho_{org}}\,\frac{p_{org,eq}}{P_s}\,\frac{q_s}{\frac{q_s}{k\,P_s}+1} \quad (1)$$

A_{sub} is the substrate area, ρ_{org} is the organic material density, $\dot{n}_{org,SH}$ is the molar flow rate of organic molecules injected into the deposition chamber by the SH. Provided that there are no cold spots between the source cell and the SH, it is reasonable to assume that the molar flow rate of organic material is conserved in this section of the system. In consequence, $\dot{n}_{org,SH}$ is equal to $\dot{n}_{org,s}$, the molar flow rate of organic molecules exiting the source cell. It is then detailed in the second identity of Equation (1), using the source cell operation equation specifically developed for OVPD in ref. [14]. In this expression, $p_{org,eq}$ is the organic material equilibrium vapor pressure at the source cell temperature, P_s is the source cell pressure, q_s is the molar flow rate of carrier gas

© 2012 WILEY-VCH Verlag GmbH & Co. KGaA, Weinheim

in the source cell and k is a constant that is related to the kinetics of evaporation. In Equation (1), the material utilization efficiency η represents the ratio of the amount organic material effectively condensed on the substrate to the amount of organic material that is injected in the chamber by the SH. This ratio results from the complex interplay between convective forces that tend to sweep the solute organic species along with the carrier gas to the pump and the diffusion of organic molecules across the carrier gas BL formed on the substrate surface.[11]

Due to the pressure drop occurring across the showerhead and the furnace piping, P_s is always somewhat higher than P_{ch} (their measured relationship is detailed in Supporting Information). This implies that the sublinear evolution of r with q_s expressed in Equation (1) becomes linear at the limit of high pressures:

$$\lim_{P_s \to \infty} r = \frac{\eta}{A_{sub}\rho_{org}} \frac{p_{org,eq}}{P_s} q_s \quad (2)$$

Equation (2) is that of a source cell operating in an equilibrium evaporation regime.[11] Upon pressure increase, the gas volume flow rate decreases and the convective transport of organic molecules out the source cell is slowed down. As a consequence, the partial pressure of organic molecules remains close to their equilibrium vapor pressure $p_{org,eq}$. This regime is technologically interesting as the amount of material convectively transported out of the source cell is only dependent on $p_{org,eq}$ and no longer on the evaporation kinetics (embodied in the factor k in Equation (1)). This equilibrium operation results in a more reproducible evaporation process in the source cell. This effect is clearly visible in Figure 2b, where the low pressure curve shows a sublinear behavior that tends to saturate due to a kinetic limit in the evaporation of source material, whereas the high pressure curve displays a linear behavior that is symptomatic of a source cell operating at equilibrium.

In order to extract the material utilization efficiency η in different pressure regimes, the curves in Figure 2b are fitted using Equation (1) and Equation (2) for respectively the low and the high pressure cases. This gives η = 26.5 ± 3.7% at P_{ch} = 1 mbar and η = 25.0 ± 0.9% at P_{ch} = 1020 mbar. These similar values for η show that this system parameter is rather independent of pressure. This independence was also observed by Lunt et al. for a different system architecture and a narrower pressure range.[15] It finds its origin in the invariance of the Peclet number Pe with pressure.[16] This unitless number represents the ratio between convective and diffusive fluxes and is defined by $Pe = UL/D$ where U is the carrier gas velocity, L is a characteristic length of the system and D is the diffusivity of organic molecules in the carrier gas. In first approximation both U and D vary as $1/P_{ch}$, causing the relative independence of Pe with pressure. In other words, as pressure rises, both the carrier gas velocity and the diffusivity of organic species decrease at the same pace. In consequence, all flow dynamics slow down and a status quo is maintained regarding the distribution of organic species in the chamber. In conclusion, the ratio of convective flux to the pump line and diffusive flux across the BL remains unaffected by a rise in P_{ch}, resulting in a constant η.

With η remaining constant, the dramatic drop of r upon a pressure increase shown in Figure 2a is only due to the increase in source cell pressure P_s. This is easily inferred from Equation (1) which gives a good fit of the data points. At high P_s, the reduced convective transport of organic molecules out of the source cell results in lower deposition rates.

In this section, we have shown how an important rise of chamber pressure P_{ch} affects the mass transport in the OVPD system. It results in a slowdown of all carrier gas flow. The source cell operates at equilibrium with a slower material pick-up. In the deposition chamber, both convective and diffusive fluxes are equally decreased, resulting in a constant material utilization efficiency η. It is reasonable to assume that a similar behavior can be expected in different OVPD system architectures such as the one presented in ref. [15].

2.2. Effect of Pressure on Pentacene Layer Morphology and Microstructure

Prior to the growth of pentacene by OVPD, silicon substrates are treated with a 5 nm thick poly-(α-methylstyrene) (PαMS) film that ensures a favorable polycrystalline growth for transistor applications.[17] As depicted in **Figure 3**a, for the chosen

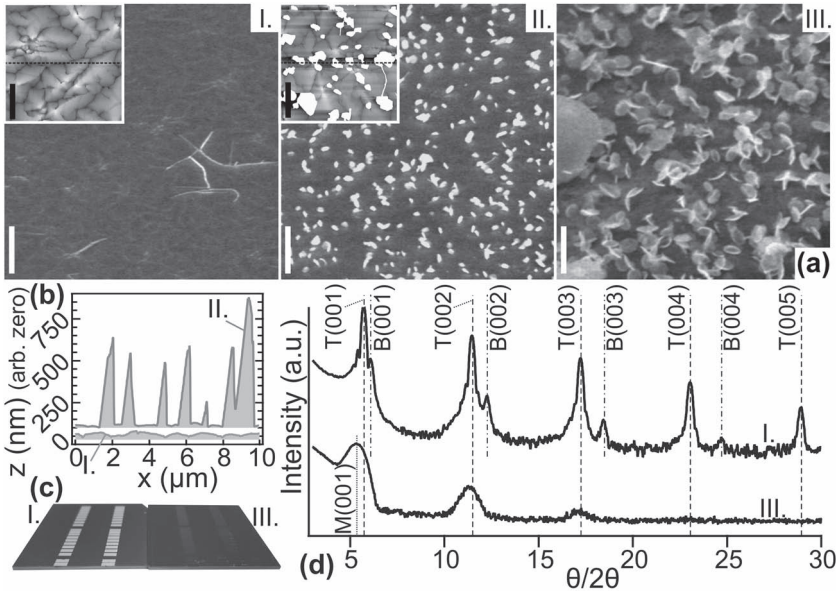

Figure 3. Three pentacene films are grown to a nominal thickness of 40 nm with the following pressures: P_{ch} = 25 ± 0.5 (I), 150 ± 3 (II) and 1000 ± 20 (III) mbar. Other growth conditions are r = 0.70 ± 0.1 Å/s, T_{sub} = 65 ° C, q_{tot} = 100 sccm. a) Morphologies by SEM and AFM (insets). Film rms roughness, extracted from the AFM images and by optical interferometry, is respectively 14, 139 and 530 nm. All scale bars are 3 μm long. b) Height profiles extracted under the central lines across AFM image of sample I and II. c) Pictures of samples I and III. The structures are the top contacts subsequently evaporated through a shadow mask to fabricate transistors. d) XRD $\theta/2\theta$ spectra of samples I and III. T and B respectively designate thin film and bulk phases of pentacene. M designates the position of a monolayer peak.

© 2012 WILEY-VCH Verlag GmbH & Co. KGaA, Weinheim

growth conditions, the increase of chamber pressure from low vacuum up to atmospheric pressure comes with an extreme layer roughening. At P_{ch} = 25 mbar (sample I), the layer morphology is that of pentacene grown by VTE, displaying terraced dendritic grains with a diameter of up to 5 µm and a rms (root mean square) roughness of 14 nm.[18] Upon pressure increase to 150 mbar (sample II), bulky crystallites with heights up to 0.8 µm are homogeneously distributed on the sample surface. In between the crystallites, a pentacene thin film resembling that of sample I is still discernible. Comparison of the AFM height profiles in Figure 3b renders well the striking roughening caused by these crystallites. Sample II has an rms roughness of 139 nm. When going to higher pressures, the crystallites become larger. Many appear as flakes rather than bulky structures, showing the onset of a two-dimensional growth mode. These flakes fully cover the surface preventing to see whether a usual thin film is formed underneath or in-between. In this case, the roughness is so important and the film so fragile that it impedes most techniques commonly used to extract roughness values. Only optical interferometry could give us an estimate rms roughness of 530 nm for sample III. This roughness is visible by eye, as the pentacene layers grown at atmospheric pressure lose all shininess and display a dull purple color (Figure 3c).

As shown by the XRD measurements of sample I and III in Figure 3d, this roughening affects the pentacene film microstructure. At low pressure, the XRD measurement of sample I resembles that of a pentacene thin film grown by VTE, displaying two polymorphs: the pentacene thin film phase (T) and the pentacene bulk phase (B).[12] It has been shown that the occurrence of the B phase depends on a number of process parameters, among which the film thickness d is predominant.[18,19] For pentacene grown on PαMS, the B phase is usually absent in thin films (d < 20 nm) whereas it is observed in sufficiently thick films. The presence of narrow and intense Bragg peaks up to the fifth order indicate good vertical ordering. On the other hand, the XRD measurement of sample III, grown near atmospheric pressure, shows only a family of three broad peaks, hinting towards a poor vertical ordering. Quite remarkably these peaks are slightly left-shifted in comparison to the T phase and correspond to an increased interlayer distance of 16.0 Å. This could be assigned to a "monolayer" (M) phase of pentacene, where unit cell parameter γ is equal to 90° and pentacene molecules are adopting a near-vertical orientation. This M phase has only been observed in single pentacene monolayers.[20,21] We speculate that this polymorph might correspond to the large flakes lying flat on the substrate.

2.3. Effect of Pressure on Pentacene Transistor Electrical Characteristics

Bottom-gate top-contact thin film transistors (TFTs) are fabricated by the growth of 30 nm of pentacene on a conductive substrate (highly doped Si) with a dielectric surface treatment (SiO_2 and PαMS), followed by the evaporation of gold through a shadowmask. We evaluate the mobility μ_{sat} and the threshold voltage V_T from TFT transfer curves measured in saturation and averaged from at least four devices per sample. We have previously

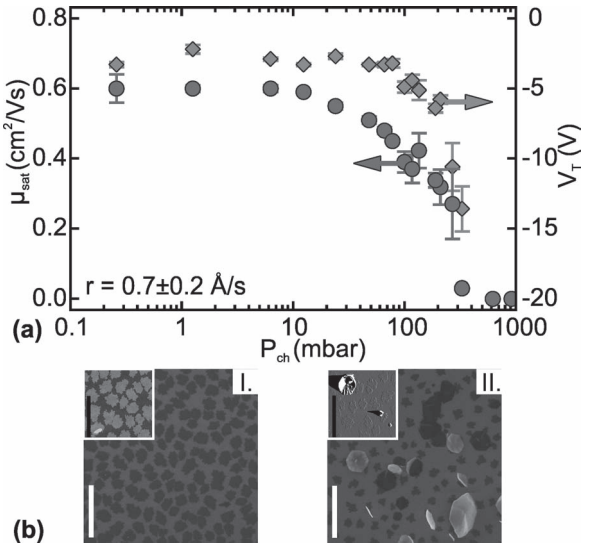

Figure 4. a) Evolution of TFT saturation mobility μ_{sat} and threshold voltage V_T with deposition pressure P_{ch}. A constant deposition rate r of 0.7 ± 0.2 Å/s is maintained by increasing T_{fur} along with P_{ch} from 230 to 290 °C. Other parameters are T_{sub} = 65 °C, q_s = 50 sccm and q_{tot} = 100 sccm. b) Pentacene sub-monolayer morphologies by SEM and AFM (inset) at a nominal coverage θ of ≈0.5. Pentacene sub-MLs are grown with the same conditions as in (a), but for a short time (8 s) and a pressure P_{ch} of 1 ± 0.02 (I) and 1000 ± 20 (II) mbar. All scale bars are 3 µm long. AFM images show the topography (I) and the gradient of topography (II).

shown in ref. [7] that pentacene TFT performances vary with r and we have observed in Figure 2a that r greatly varies with P_{ch}. Special care must therefore be taken to decouple the effects of these two parameters on TFT characteristics. **Figure 4**a shows the evolution of μ_{sat} and V_T with P_{ch} on a series of samples grown with a deposition rate r = 0.7 ± 0.2 Å/s. A stable r is achieved over a wide pressure span thanks to an increase of T_{fur} in parallel to that of P_{ch}. For the chosen experimental conditions (r, q_{tot}, q_s, T_{sub}), Figure 4a reveals a rapid degradation of pentacene TFT performances with an increase of pressure. At P_{ch} below 20 mbar, transistors are well behaved, with μ_{sat} ≈ 0.6 cm²/Vs and V_T ≈ −4 V. Such performance is typical for the chosen deposition rate and the substrate pretreatment.[13] Upon pressure increase, μ_{sat} first starts to degrade (at P_{ch} > 20 mbar), then V_T strongly decreases (at P_{ch} > 150 mbar). Both effects hint towards the increased presence of traps in the transistor channel. At P_{ch} > 350 mbar, transistor behavior is no longer observed in our devices (μ_{sat} is set to 0 cm²/Vs and V_T is set to V_{DS} = −20 V).

In order to get a better understanding of this rapid TFT degradation with the rise in pressure, we characterized the morphology of very thin pentacene layers grown in the same conditions as that of the functional films. Indeed, in the channel of a TFT, the first few pentacene monolayers (MLs) formed on the gate dielectric are the region where charge accumulates and is laterally transported.[22–24] Practically, we obtained sub-ML growth by using the same process conditions as that used to generate the data in Figure 4a, and by interrupting growth at a very early stage (8 s for r = 0.7 Å/s). The morphology of such layers deposited at low (I) and high (II) pressure is shown in

© 2012 WILEY-VCH Verlag GmbH & Co. KGaA, Weinheim

Figure 4b. At P_{ch} = 1 mbar, the sub-ML pentacene islands have a height measured by AFM of about 15 Å, corresponding to the height (along the c axis) of pentacene unit cells.[25] Clearly, pentacene sub-ML formation by OVPD obeys the diffusion-limited aggregation model and resembles much that observed in VTE.[26,27] This is remarkable considering the presence of a background gas that influences most of the microscopic events taking place at this stage of growth (e.g., molecular adsorption, desorption, surface diffusion, aggregation). On the other hand, at atmospheric pressure, traditional sub-ML islands are still present but their size and density are lower. On top of these islands, large needles and flakes are randomly distributed. Upon further growth (shown in Figure S2 in the Supporting Information), the growth and coalescence of sub-ML islands is greatly impeded by the increasing density and size of these crystallites. They consume most of the new-coming molecules, preventing the proper formation of the first ML and, consequently, also of the next MLs. Such structural defects are known to form charge carrier traps.[28] Moreover, by preventing proper island coalescence into a continuous film, they yield longer charge percolation paths.[29] Both effects can explain the degradation in transistor characteristics μ_{sat} and V_T with pressure increase observed in Figure 4a.

2.4. Origin of Pentacene Layer Roughening at Atmospheric Pressure

The formation of crystallites at high pressure is undesirable as this phenomenon delivers films with unpractical roughness and poor electrical characteristics. We therefore try to understand this phenomenon in order to devise ways to suppress it.

As can be seen in Figure 4b, the hexagonal shape of the large flakes is close to an equilibrium shape of pentacene crystals.[30] Moreover these flakes are randomly distributed on the substrate, some lying flat, others lying on their edge. Finally, the crystallites have a very weak binding to the substrate and can be partially blown away using a nitrogen gun. In fact the formation of the high-pressure crystallites appears to be quite independent of the substrate. This is contrary to what is usually observed in the growth of small organic molecules where the substrate always somewhat templates crystal growth. We therefore conclude that the crystallites are formed away from the substrate, in the carrier gas BL, as a result of a gas phase nucleation (GPN) event.

In the absence of a substrate and of impurities in the gas phase, GPN in the OVPD chamber is a case of homogeneous nucleation whose treatment by the classical nucleation theory (CNT) is straightforward. One must however keep in mind that this theory reaches its limits when considering far from equilibrium systems and small critical nuclei. In the following, we try to understand how an increased chamber pressure gives rise to GPN by observing the effect of P_{ch} on two important nucleation markers: the supersaturation $\Delta\mu$ and the nucleation rate J. We follow the CNT description by Markov to define these two parameters.[31]

The supersaturation $\Delta\mu$ is the driving force for a transition from the gas to the solid phase. Hence, its value informs about the thermodynamic possibility to homogeneously nucleate crystals.[32] $\Delta\mu$ can be analytically evaluated using the following equation:

$$\Delta\mu = k_B T \ln\left(\frac{p_{org}}{p_{org,eq}}\right) \quad (3)$$

where T is the local temperature, p_{org} is the partial pressure of organic molecules and $p_{org,eq}$ is their equilibrium vapor pressure at T. In CNT, the size r^* of critical nuclei is a function of $1/\Delta\mu$. Therefore, at thermodynamic equilibrium, $\Delta\mu = 0$ and r^* takes an infinite value: No homogeneous nucleation can occur. In conclusion, GPN requires a strictly positive value of $\Delta\mu$ to take place.

The rate of nucleation J is the rate of formation of stable nuclei through the addition of single molecules to critical nuclei. It is mathematically formalized by:

$$J = \omega^* \Gamma N^* = \omega^* \Gamma N \exp\left(-\frac{\Delta G^*}{kT}\right) \quad (4)$$

where ω^* is the frequency of attachment of molecules to critical nuclei, Γ is known as the Zeldovich factor that accounts for deviations from the equilibrium state and N^* is the equilibrium concentration of critical nuclei. The latter parameter is a function of N, the concentration of single molecules in the gas phase, and of ΔG^*, the free Gibbs energy of formation of critical nuclei. It can be shown (see Supporting Information) that J is proportional to the square of the organic partial pressure $p_{org}{}^2$ (through $\omega^*\Gamma N$) and that J experiences a very rapid increase once $\Delta\mu$ rises above a certain threshold value (through the free Gibbs energy term). In order to understand the full effect of P_{ch} on J, we need to understand how p_{org} and $\Delta\mu$ evolve in the OVPD chamber upon pressure change. This can be done using a one-dimensional (1D) analytical model that uses Equation (3) to quantitatively evaluate $\Delta\mu$ along a vertical axis joining the SH to the substrate surface. In the following paragraph, we describe how $p_{org,eq}$ and p_{org} are evaluated along the considered vertical axis.

The diagram in **Figure 5** shows a cross-section of the OVPD chamber close to the edge of the susceptor and gives an idealized view of the carrier gas flow lines in this geometry. In order to avoid edge effects, the 1D model axis shown in the diagram is taken far away from this edge, along the central axis of the cylindrical chamber. Assuming in first approximation a linear temperature gradient going from the hot showerhead down to the cooled substrate, one can calculate $p_{org,eq}$ as a function of chamber height h, using the Clausius-Clapeyron equation. This is done for pentacene using the parameters given in ref. [33]. In order to evaluate p_{org} along the 1D model axis, we assume that the chamber is divided in two regions (see Figure 5): A convective region located between the SH surface and the top of the BL where p_{org} is constant, equal to its value at the chamber inlet $p_{org,SH}$; and a diffusive region located between the top of the BL and the substrate surface, where p_{org} linearly drops from $p_{org,SH}$ down to $p_{org,sub}$, the partial pressure that the thermalized gas of organic material directly applies on the substrate surface. The boundary between the two regions is set by the BL thickness δ_{BL}, which is independent from chamber pressure and is evaluated to be δ_{BL} = 14 mm for the considered conditions and geometry (see Supporting Information).

© 2012 WILEY-VCH Verlag GmbH & Co. KGaA, Weinheim

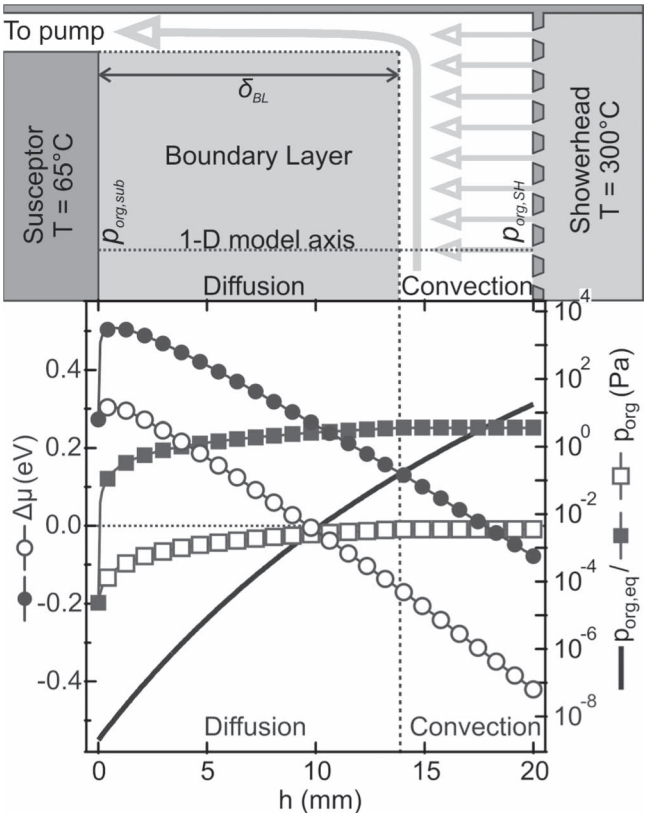

Figure 5. Diagram: Schematic cross-section of the OVPD chamber close to edge of the susceptor. Graph: Evolution of supersaturation $\Delta\mu$ (circles), organic partial pressure p_{org} (squares) and organic equilibrium vapor pressure $p_{org,eq}$ (line) at high (1020 mbar- full symbols) and low (1 mbar- open symbols) pressures, as a functions of chamber height. $h = 0$ and 20 mm, respectively, correspond to substrate and showerhead surfaces. The conditions are the ones used to produce samples I and II in Figure 4b, (see Table 1).

As we have shown in section 2.1, the chamber pressure hardly affects chamber efficiency η. As a consequence, for a same value of r, Equation (1) gives an organic molar flow rate at the chamber inlet $\dot{n}_{org,SH}$ that is independent of pressure: In order to maintain a constant rate as pressure varies, a same amount of material is injected into the OVPD chamber by the SH. The step from molar flow rates to partial pressure is taken by writing the molar fraction of organic material at the chamber inlet $X_{org,SsH}$:

$$X_{org,SH} = \frac{p_{org,SH}}{P_{ch}} = \frac{\dot{n}_{org,SH}}{\dot{n}_{org,SH} + \dot{n}_{cg,SH}} \quad (5)$$

where $\dot{n}_{cg,SH}$ is the molar flow rate of carrier gas injected by the SH. It corresponds to the total carrier gas flow rate q_{tot} through a unit change. Equation (5) shows that for a constant ratio $X_{org,SH}$ (corresponding to a constant r), an increase of P_{ch} by 3 orders of magnitude results in equivalent increase of $p_{org,SH}$. In other words, as the chamber pressure rises, carrier gas velocity drops, resulting in less convective transport and higher concentration of organic material within the chamber.

Table 1. Numerical values calculated from Equation 1, 3, 5 and 6 using the conditions used to produce samples I and II in Figure 4b, namely: T_{SH} = 300 °C, T_{sub} = 65 °C, q_{tot} = 100 sccm.

Sample	P_{ch} [mbar]	r [Å/s]	$\dot{n}_{org,SH}$ [mole/s]	$p_{org,SH}$ [Pa]	$p_{org,sub}$ [Pa]	$\Delta\mu_{max}$ [eV]
I	1	0.7	2.6×10^{-9}	3.6×10^{-3}	2.4×10^{-5}	0.29
II	1020	0.7	2.6×10^{-9}	3.6	2.4×10^{-5}	0.50

The last parameter of our model, $p_{org,sub}$, is evaluated from the deposition rate r using the kinetic theory of gas:[30]

$$P_{org,sub} = \sqrt{2\pi\, M_{org}\, R T_{sub} r \rho_{org}} \quad (6)$$

where M_{org} is the molar mass of organic material. Equation (6) gives the partial pressure of organic material in the layer of thermalized gas directly in contact with the sample that is necessary to maintain a net flux of $r\rho_{org}$ on the substrate. **Table 1** shows numerical values of $\dot{n}_{org,SH}$, $p_{org,SH}$ and $p_{org,sub}$ that are evaluated using Equations (1), (5) and (6) for two different chamber pressures: 1 and 1020 mbar. These values are calculated with the experimental conditions used in the growth of sample I and II of Figure 4b. The values given in Table 1 are used to parameterize the model described above and to produce the mapping shown in Figure 5 of p_{org} (squares) and $\Delta\mu$ (circles) in the OVPD chamber for the two growths shown in Figure 4b. $p_{org,eq}$ is indicated as well in Figure 5 (line), showing that the vapor pressure drops by 10 orders of magnitude between the showerhead (x = 20 mm in Figure 5) and the substrate (x = 0 mm), corresponding to a temperature drop from T = 300 °C to T = 65 °C. With p_{org} varying by only two orders of magnitude over the same distance, this dramatic drop of $p_{org,eq}$ is responsible for the almost linear increase of $\Delta\mu$ when approaching the substrate. $\Delta\mu$ peaks at a height h ≈ 0.8 mm above the substrate surface. In the immediate vicinity of the surface, p_{org} linearly drops to $p_{org,sub} = 2.4\times10^{-5}$ Pa calculated using Equation (6) with r = 0.7 Å/s and $\Delta\mu$ converges to a finite value of 0.27 eV. As shown in Table 1, in the low pressure case, $\Delta\mu$ reaches a peak values $\Delta\mu_{max}$ of 0.29 eV, close to its boundary value at the substrate. On the other hand, in the high pressure case, $\Delta\mu$ peaks at 0.50 eV, which, considering the exponential nature of this parameter, corresponds to a tremendous driving force for phase change. Finally, upon pressure rise, the thickness of the region where $\Delta\mu > 0$ and where GPN is therefore thermodynamically allowed is almost doubled, from h ≈ 9 mm up to h ≈ 17 mm thick. As at higher pressures gas flow velocities are lower, the system is given a lot more time and space for GPN to occur.

To state whether or not GPN will occur, we need to reconsider the nucleation rate J in the light of this model. As shown by Figure 5, an increase of chamber pressure P_{ch} by three orders of magnitude results in a proportional increase of p_{org} and in a significant increase of $\Delta\mu$ across the whole chamber. In this case, considering the dependencies of J stated above, the homogeneous nucleation rate J will rise by at least six orders of magnitude thanks to its proportionality to p_{org}^2. The effect of $\Delta\mu$ increase on J is more difficult to assess, as it requires solving Equation (4) in order to evaluate the threshold value of $\Delta\mu$ above which the energetic barrier for the formation of critical nuclei

© 2012 WILEY-VCH Verlag GmbH & Co. KGaA, Weinheim

is crossed. This we leave to further work but we speculate that the significant rise in $\Delta\mu$ is enough to cross this threshold value and to enable GPN. In conclusion, we have qualitatively shown in this discussion how an increase in chamber pressure can give rise to gas phase nucleation. This happens thanks to the collective enhancement of the molecular collision rate, molecular concentration and supersaturation.

2.5. Suppression of Gas Phase Nucleation

Considering the discussion above, there are two routes to achieve the suppression of GPN at high pressure. The first route is a decrease of the organic partial pressure p_{org} in the OVPD chamber. This will impact the supersaturation $\Delta\mu$, the attachment frequency ω^* and the equilibrium concentration of single molecules N. All three effects will combine to decrease the nucleation rate J. Considering Equation (5), lower p_{org} can be experimentally achieved either by decreasing $\dot{n}_{org,SH}$ using lower T_{fur} or q_s, hence lower deposition rates r, or by increasing $\dot{n}_{cg,SH}$ using higher dilution flow rates to increase the total flow rate q_{tot}. The second route is an increase of the equilibrium vapor pressure $p_{org,eq}$ of organic material within the OVPD chamber. This can be experimentally achieved by increasing the substrate temperature T_{sub} and therefore limit the drop in $p_{org,eq}$ across the OVPD chamber. As $\Delta\mu$ reaches its maximum close to the substrate, significantly lower peak values $\Delta\mu_{max}$ are expected with higher T_{sub}.

Fixing the deposition rate r to a low value of 0.15 Å/s, pentacene was grown at atmospheric pressure with a systematic variation of substrate temperature T_{sub} and total flow rate q_{tot}. The morphology of these thin films is shown in **Figure 6**, and reveals two trends: The variation of T_{sub} over an interval of

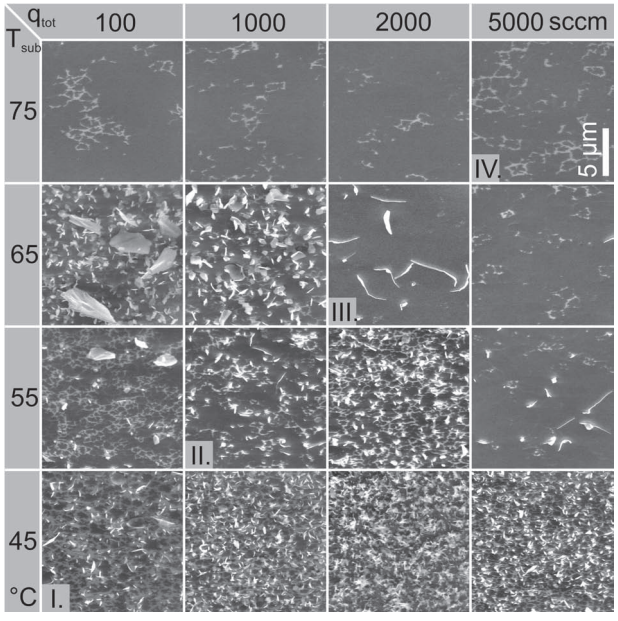

Figure 6. Morphological evolution with T_{sub} and q_{tot} of ≈30 nm thick pentacene films imaged by SEM. All films are grown at atmospheric pressure (P_{ch} = 1020 ± 20 mbar) and low rate (r = 0.15 ± 0.05 Å/s).

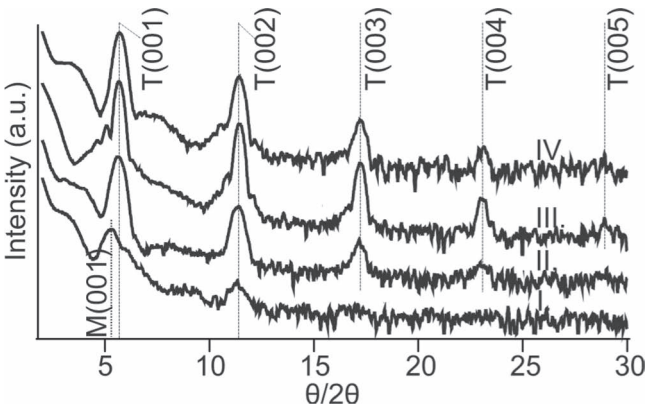

Figure 7. XRD $\theta/2\theta$ measurements of 30 nm thick pentacene films shown along the diagonal of Figure 6.

30 °C has a profound impact on the layer morphology: lower T_{sub} results in a high density of small crystallites, whereas GPN is totally suppressed at higher T_{sub}. As expected, the effect of T_{sub} on $\Delta\mu$ via $p_{org,eq}$ is important, resulting in a large variation of the nucleation rates J over a limited T_{sub} range. This clearly shows that GPN is triggered by a sharp temperature drop of process gas. The influence of q_{tot} variation on morphology, also visible in Figure 6, is less radical but does reveal a suppression of GPN at intermediate T_{sub}. Interestingly, the largest crystallites are formed at the lowest q_{tot} of 100 sccm, which is counterintuitive as these conditions correspond to high p_{org}, hence higher J. This could be a dynamic effect: At lower q_{tot}, gas velocity is decreased, giving more time for the crystallites to grow once they have nucleated.

In order to assess the microstructure of these pentacene layers, **Figure 7** shows the XRD measurements of samples lying along the diagonal of fastest morphological change in Figure 6. Sample I, grown at low T_{sub} and q_{tot}, has a disordered pentacene film as is prevalent by the presence of weak and very broad Bragg peaks, which are slightly left-shifted with respect to the T phase of pentacene and therefore could be assigned to the M polymorph that was already seen in Figure 3d. Upon an increase of T_{sub} and q_{tot}, the crystalline order improves and samples II, III and IV show diffraction peaks corresponding to the T phase of pentacene. These are less intense in sample II as the morphology of this sample reveals many gas phase nucleated crystallites that disrupt the good vertical ordering of pentacene layers. Note that the best out-of-plane ordering is seen for sample III and not for sample IV. The latter is grown in conditions that place a high thermal load on the substrate, bringing its temperature close to the glass transition temperature T_g of the polymeric dielectric used to pretreat the substrate. It is a known fact that good ordering of pentacene on PαMS suffers if T_{sub} is too close to this T_g threshold,[34] which could explain the decreased vertical ordering in sample IV. Finally the absence of the pentacene B-phase from all spectra in Figure 7 can be explained by the lower film thickness used in this experimental set compared to Figure 3d.

Next, the effect of our GPN suppression strategies on pentacene TFT characteristics is evaluated. To that end, the processing parameters r, q_{tot} and T_{sub} are separately varied around a pivot set

© 2012 WILEY-VCH Verlag GmbH & Co. KGaA, Weinheim

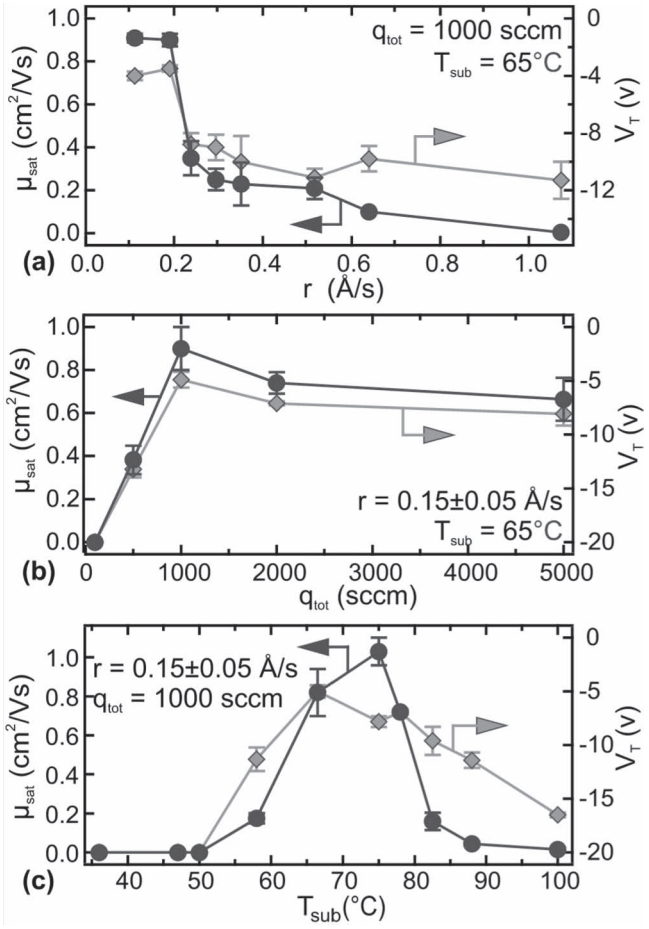

Figure 8. Evolution of TFT saturation mobility μ_{sat} and threshold voltage V_T with pentacene growth conditions at atmospheric pressure. a) Deposition rate variation. b) Total carrier gas flow rate variation. c) Substrate temperature variation.

of standard conditions, namely $r = 0.15$ Å/s, $q_{tot} = 1000$ sccm, a $T_{sub} = 65$ °C and $P_{ch} = 1020$ mbar. These standard conditions are regularly repeated in order to ensure the run-to-run reproducibility of the process. The transistor structure is the same as the one used to produce Figure 4. As can be seen from the output of this study shown in **Figure 8**, the dramatic degradation of transistor performance upon pressure increase seen in Figure 4a can be effectively avoided at atmospheric pressure by adapting the processing conditions. First, lowering the deposition rate r (Figure 8a) is essential. Irrespective of the other processing conditions, we were not able to produce films of good electrical quality unless r was lowered below a threshold value of about 0.2 Å/s. Secondly, an increase of q_{tot} (Figure 8b) is also important as films grown at 100 sccm deliver poor electrical properties. However, above 2000 sccm, pentacene film properties start to degrade slowly. As mentioned earlier, this is probably caused by the increased thermal load on the PαMS substrate pretreatment. This thermal load issue is also the reason behind the rapid degradation of pentacene TFT characteristics for films grown with a T_{sub} higher than 80 °C (Figure 8c). On the other hand, increasing the temperature appears to very effectively promote pentacene electrical properties.

It is clear from Figure 8 that our GPN suppression strategies are effectively limiting the detrimental effect of GPN on the electrical characteristics of pentacene grown at atmospheric pressure. The standard conditions defined above deliver pentacene films whose TFTs characteristics, $\mu_{sat} \approx 0.9$ cm²/Vs and $V_T \approx -4$ V, are of excellent quality. Note that with these conditions, GPN still occurs, giving a rough pentacene layer as can be seen in Figure 6. However, GPN is delayed long enough so that it doesn't disrupt the formation of the first pentacene ML, ensuring a successful lateral charge transport within this layer. This is clearly visible in Figure S3 (see Supporting Information) that shows SEM images of a sub-ML and of a 30 nm thick pentacene film grown with optimal conditions for transistor applications. It also shows that the XRD measurement obtained on the thicker film is similar to that of sample III in Figure 7, indicating a favorable microstructure despite the apparent roughness of this layer.

2.6. High-Quality TFTs Based on Pentacene Grown at Atmospheric Pressure

The successful atmospheric pressure processing window defined in the previous section is used to reproducibly deposit high-quality pentacene films at atmospheric pressure. **Figure 9**a and b respectively show output and transfer curves of bottom-gate top-contact TFTs based on pentacene layers processed by OVPD at atmospheric pressure on PαMS. With an onset voltage close to 0 V, a low threshold voltage, a high saturation mobility, a sub-threshold slope below 0.4 V/dec, a negligible hysteresis and a I_{on}/I_{off} ratio consistently above 10^6, these characteristics are of excellent quality and are comparable to previous results based on similar TFT structures.[7] Moreover, Figure 9b, shows superimposed transfer curves of 38 TFTs measured over eight different samples whose pentacene was grown at atmospheric pressure during different runs. The spread in performances remains low ($\mu_{sat} = 0.90 \pm 0.07$ cm²/Vs and $V_T = -5.2 \pm 1.5$ V), indicating the good electrical uniformity over a sample surface and the good run-to-run reproducibility of these layers.

These process conditions are also used to apply pentacene as the active layer of inverters and simple circuits fabricated with our existing TFT baseline technology that is based on bottom-contact transistors on a PEN-foil (polyethylenenaphthalate).[35] Inverters output curves are displayed in Figure 9c, showing that in this technology, the 0-VGS configuration delivers successful p-type logic. Figure 9d shows the output curve of a 19-stage ring oscillators based on this logic. With a 25 V supply voltage, this circuit oscillates at a 500 Hz frequency corresponding to a stage delay of 51 µs. The successful operation of such a device requires the simultaneous operation of 40 pentacene transistors, again showing the good uniformity of pentacene electrical characteristics over the surface of a sample.

3. Conclusions

Because of its use of a carrier gas, the OVPD technology possesses a supplementary process parameter to influence growth: the chamber pressure P_{ch}. Using an OVPD tool adapted to

© 2012 WILEY-VCH Verlag GmbH & Co. KGaA, Weinheim

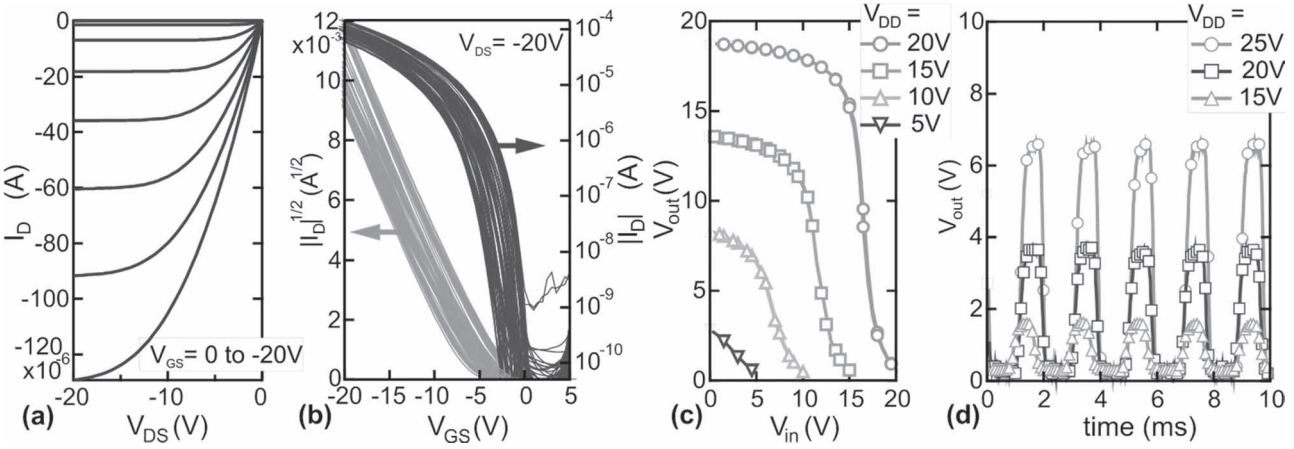

Figure 9. Electrical characteristics of pentacene layers grown at atmospheric pressure. a) Output curve of a top contact TFT. b) Superimposed transfer curves of 38 top contact TFTs measured over 8 samples. c) 0–V_{GS} inverters. d) Output of a 19-stage ring oscillator based on 0-VGS logic. Pentacene growth conditions are: P_{ch} = 1020 ± 20 mbar, 0.1 < r < 0.2 Å/s, q_{tot} = 1000 sccm, T_{fur} = 260 ± 5 °C and T_{sub} = 65 °C.

achieve pressure variations over 4 decades, from 0.1 mbar up to atmospheric pressure, we explore the influence of large P_{ch} variation over pentacene growth.

Considering the effect of P_{ch} on mass transport in the OVPD tool, we observe that this parameter only mildly affects material utilization efficiency which remains close to 25% over the whole pressure span. Moreover, at high pressure, the evaporation process in the source cell appears to occur at equilibrium, thanks to a lowered carrier gas velocity. This leads to reproducible source operation but also gives lower evaporated fluxes of organic molecules, requiring higher furnace temperatures to keep acceptable deposition rates.

Upon pressure increase, we observe an extreme roughening of pentacene layers. This phenomenon is assigned to a gas phase nucleation (GPN) process in which pentacene crystals homogeneously nucleate in the chamber atmosphere and "snow" down on the sample. As GPN is very detrimental for layer morphology and electrical characteristics, we study its origin in order to devise ways to suppress it. Through a quantitative mapping of the partial pressure of organic molecules and their supersaturation across the OVPD chamber, we show that an increase in P_{ch} leads to a great rise in GPN rate. This is due to the collective enhancement of the molecular collision rate, molecular concentration and supersaturation in the atmosphere above the substrate.

This study gives the keys to suppress GPN at atmospheric pressure. Experimentally this can be achieved by lowering the deposition rate, increasing the dilution of organic molecules in the carrier gas and increasing the substrate temperature. We show that these three strategies are successful and can be used to define a process window for the growth of high-quality pentacene films at atmospheric pressure.

Using these conditions we reproducibly fabricate state-of-the-art pentacene thin film transistors. These layers are also used as the active layer of simple p-type circuits. We demonstrate a working 19-stage ring oscillator based on pentacene grown by OVPD at atmospheric pressure.

4. Experimental Section

The OVPD system used in this study was a homebuilt system presented in ref. [13,14]. It was equipped with a 75 mm diameter hot showerhead that uniformly spreads the carrier gas onto the water cooled 60 mm diameter copper susceptor located 20 mm underneath. This design ensured a stable substrate temperature T_{sub} controlled between 25 and 105 °C as measured by a thermocouple inserted at the bottom of the copper susceptor and probing the temperature close to its surface. Sample loading and unloading was facilitated by the use of a loadlock, ensuring a high-throughput of samples. A large pressure range was accessible because of the use of a throttle valve at low pressure and of a removable constriction in the pump line at higher pressures. The pressure was finely adjusted to a stable value by regulating the amount of supplementary nitrogen injected into the pump line. Chamber pressure P_{ch} was accurately measured over a large range using both a capacitance gauge and a convection Pirani gauge directly attached to a cold port of the deposition chamber. Mass flow controllers (MFC) were used for nitrogen injection. Assuming nitrogen is an ideal gas, the following conversion factor was used to convert sccm to SI units: 1 $sccm_{N2} = 2.083 \times 10^{-8}$ kgs^{-1}.

Pentacene was purchased from Aldrich and used as such without further purification. It was placed in the source cell and evaporated using a furnace temperature T_{fur} ranging from 230 to 290 °C and a pre-heated nitrogen carrier gas flow rate q_s varying between 25 and 500 sccm. In order to ensure a good functioning of the showerhead, this source flow is diluted with supplementary nitrogen to fix the total carrier gas flow rate q_{tot} between 100 and 5000 sccm.

Substrates used in this study were either highly doped 2 × 2 cm^2 silicon wafers, or highly doped 2 × 2 cm^2 silicon wafers with a thermally grown SiO_2 layer of 120 nm thickness. The substrates were cleaned as follows: 2 min dip in DI water/2 min dip in acetone at 40 °C/2 min dip in isopropanol at 40 °C/2 min exposure to an O_2-plasma. When necessary, the wafer was then treated with PαMS as follows: poly-(α-methylstyrene) (MW > 150 000) was purchased from Aldrich. It was dissolved in toluene to give a 0.1% weight solution that was spin-coated onto the wafer at 4000 rpm for 30 s. The wafer was then allowed to dry on a hot plate for 2 min at 120 °C. Depending on our characterization needs, three types of substrates were prepared: i) for SEM (and AFM) characterization, including sub-MLs of pentacene: substrate was Si n++/PαMS; ii) for thickness characterization by Ellipsometry: substrate was Si n++/SiO_2; and iii) for transistors, XRD and AFM: substrate was Si n++/SiO_2/PαMS.

© 2012 WILEY-VCH Verlag GmbH & Co. KGaA, Weinheim

The characterization of the samples was carried out with the following techniques. SEM images were acquired using a Philips XL30 and a FEI Nova NanoSem. The AFM was an Agilent 5100 operated in tapping mode. Ellipsometric measurements were carried out with a variable angle spectroscopic ellipsometer GESP-5 from Sopra. The $\theta/2\theta$ XRD measurements were performed with a PANalytical X´Pert Pro Materials Research Diffractometer using Cu Kα radiation.

Transistors were fabricated via the evaporation of 100 nm gold through a shadowmask onto an appropriate sample. This defines top source and drain electrodes with a channel width and length of respectively 2000 and 50 µm. Devices were characterized in a nitrogen filled glovebox ([O_2] < 1 ppm, [H_2O] < 1 ppm), using an Agilent 4156 parameter analyzer. Transistor mobility and threshold voltages as well as other electrical characteristics were extracted from the transistor transfer curves measured in saturation using methods described in ref. [36].

P-type circuits were based on bottom-contact transistors fabricated on a PEN-foil using 200 nm of cross-linked PVP as a gate dielectric and Au source-drain contacts with a channel-length of 10 µm. After growth, pentacene was covered with 200 nm parylene-C and patterned using an orthogonal resist, achieving off-currents below 10 pA.

Supporting Information

Supporting Information is available from the Wiley Online Library or from the author.

Acknowledgements

C.R. would like to acknowledge Prof. S. R. Forrest and the Belgian American Educational Foundation for allocating resources during the redaction of this paper. K. V. acknowledges the Institute for the Promotion of Innovation through Science and Technology in Flanders (IWT-Vlaanderen) for financial support. The authors acknowledge financial support of EC-funded project Polaric (FP7-247978).

Received: March 29, 2012
Revised: June 21, 2012
Published online: July 27, 2012

[1] S. Kowarik, A. Gerlach, F. Schreiber, *J. Phys.: Condens. Matter* **2008**, *20*, 184005.
[2] S. R. Forrest, *Nature* **2004**, *428*, 911.
[3] M. Baldo, M. Deutsch, P. Burrows, H. Gossenberger, M. Gerstenberg, V. Ban, S. Forrest, *Adv. Mater.* **1998**, *10*, 1505.
[4] OVPD is a technology by UDC exclusively licensed to AIXTRON for equipment manufacturing. The term OVPD is a trademark of AIXTRON.
[5] F. Lindla, M. Boesing, C. Zimmermann, F. Jessen, P. van Gemmern, D. Bertram, D. Keiper, N. Meyer, M. Heuken, H. Kalisch, R. H. Jansen, *Appl. Phys. Lett.* **2009**, *95*, 213305.
[6] F. Yang, M. Shtein, S. R. Forrest, *J. Appl. Phys.* **2005**, *98*, 014906.
[7] C. Rolin, K. Vasseur, J. Genoe, P. Heremans, *Org. Electron.* **2010**, *11*, 100.
[8] M. Shtein, P. Peumans, J. B. Benziger, S. R. Forrest, *Adv. Mater.* **2004**, *16*, 1615.
[9] G. J. McGraw, D. L. Peters, S. R. Forrest, *Appl. Phys. Lett.* **2011**, *98*, 013302.
[10] S. Biswas, K. P. Pipe, M. Shtein, *Appl. Phys. Lett.* **2010**, *96*, 263301.
[11] M. Shtein, H. F. Gossenberger, J. B. Benziger, S. R. Forrest, *J. Appl. Phys.* **2001**, *89*, 1470.
[12] M. Kitamura, Y. Arakawa, *J. Phys.: Condens. Matter* **2008**, *20*, 184011.
[13] C. Rolin, S. Steudel, K. Myny, D. Cheyns, S. Verlaak, J. Genoe, P. Heremans, *Appl. Phys. Lett.* **2006**, *89*, 203502.
[14] C. Rolin, K. Vasseur, S. Schols, M. Jouk, G. Duhoux, R. Müller, J. Genoe, P. Heremans, *Appl. Phys. Lett.* **2008**, *93*, 033305.
[15] R. R. Lunt, B. E. Lassiter, J. B. Benziger, S. R. Forrest, *Appl. Phys. Lett.* **2009**, *95*, 233305.
[16] D. M. Dobkin, M. K. Zuraw, *Principles of Chemical Vapor Deposition: What's Going on Inside the Reactor*, Kluwer Academic, Dordrecht London **2003**.
[17] T. W. Kelley, P. F. Baude, C. Gerlach, D. E. Ender, D. Muyres, M. A. Haase, D. E. Vogel, S. D. Theiss, *Chem. Mater.* **2004**, *16*, 4413.
[18] A. Brillante, I. Bilotti, R. Della Valle, E. Venuti, A. Girlando, M. Masino, F. Liscio, S. Milita, C. Albonetti, P. D'angelo, A. Shehu, F. Biscarini, *Phys. Rev. B* **2012**, *85*, 195308.
[19] T. Kakudate, N. Yoshimoto, Y. Saito, *Appl. Phys. Lett.* **2007**, *90*, 081903.
[20] S. E. Fritz, S. M. Martin, C. D. Frisbie, M. D. Ward, M. F. Toney, *J. Am. Chem. Soc.* **2004**, *126*, 4084.
[21] S. C. B. Mannsfeld, A. Virkar, C. Reese, M. F. Toney, Z. Bao, *Adv. Mater.* **2009**, *21*, 2294.
[22] F. Dinelli, M. Murgia, P. Levy, M. Cavallini, F. Biscarini, D. de Leeuw, *Phys. Rev. Lett.* **2004**, *92*, 116802.
[23] R. Ruiz, A. Papadimitratos, A. C. Mayer, G. G. Malliaras, *Adv. Mater.* **2005**, *17*, 1795.
[24] A. Shehu, S. Quiroga, P. D'Angelo, C. Albonetti, F. Borgatti, M. Murgia, A. Scorzoni, P. Stoliar, F. Biscarini, *Phys. Rev. Lett.* **2010**, *104*, 246602.
[25] R. Ruiz, A. C. Mayer, G. G. Malliaras, B. Nickel, G. Scoles, A. Kazimirov, H. Kim, R. L. Headrick, Z. Islam, *Appl. Phys. Lett.* **2004**, *85*, 4926.
[26] R. Ruiz, B. Nickel, N. Koch, L. Feldman, R. Haglund, A. Kahn, F. Family, G. Scoles, *Phys. Rev. Lett.* **2003**, *91*, 136102.
[27] B. Stadlober, U. Haas, H. Maresch, A. Haase, *Phys. Rev. B* **2006**, *74*, 165302.
[28] S. Verlaak, P. Heremans, *Phys. Rev. B* **2007**, *75*, 115127.
[29] A. Di Carlo, F. Piacenza, A. Bolognesi, B. Stadlober, H. Maresch, *Appl. Phys. Lett.* **2005**, *86*, 263501.
[30] S. Verlaak, S. Steudel, P. Heremans, D. Janssen, M. Deleuze, *Phys. Rev. B* **2003**, *68*, 195409.
[31] I. Markov, *Crystal Growth for Beginners: Fundamentals of Nucleation, Crystal Growth and Epitaxy*, World Scientific, River Edge, NJ **2003**.
[32] C. Ratsch, J. A. Venables, *J. Vac. Sci. Technol. A* **2003**, *21*, S96.
[33] N. Wakayama, H. Inokuchi, *Bull. Chem. Soc. Jpn.* **1967**, *40*, 2267.
[34] C. Kim, A. Facchetti, T. J. Marks, *Science* **2007**, *318*, 76.
[35] C. Rolin, S. Steudel, P. Vicca, J. Genoe, P. Heremans, *Appl. Phys. Express* **2009**, *2*, 086503.
[36] G. Horowitz, *Adv. Mater.* **1998**, *10*, 365.

© 2012 WILEY-VCH Verlag GmbH & Co. KGaA, Weinheim